DRAFT: ILC EXTRACTION LINE FOR 14 MRAD CROSSING ANGLE*

Abstract

The earlier studies of the ILC extraction line for 20 mrad and 2 mrad crossing angle options [1]-[5] showed that the 20 mrad design has the advantage of a simpler beamline and lower extraction beam losses because of the independent incoming and extraction optics. However, the large crossing angle requires the use of a crab cavity correction, and increases the synchrotron radiation in the solenoid and the detector background due to backscattering. To reduce these effects, an attempt has been made to minimize the crossing angle while keeping the extraction and incoming lines separate. A new quadrupole design near IP has been proposed which allows to reduce the crossing angle to 14 mrad. The optics design and results of tracking and background simulations for the 14 mrad extraction line are presented.

INTRODUCTION

To be included ...

OPTICS

The 14 mrad extraction optics is similar to the 20 mrad design [4] with a few differences described below. In the 20 mrad design, the first incoming and extraction quadrupoles are placed at the same distance, s = 3.51 m after IP. This is based on the superconducting (SC) compact quadrupole design [6] which makes possible the side-by-side quadrupoles in the independent cryostats with a small 70 mm horizontal separation. However, further reduction of the separation is not advisable in this option since it is technically risky and may increase the residual field near IP.

The proposed solution for a smaller crossing angle was to move the first extraction quadrupole away from IP and behind the first incoming quadrupole QD0. In this case, the separation between the QD0 and the extraction beam pipe can be reduced for a smaller crossing angle. The schematic of the 14 mrad crossing with the nearest to IP incoming and extraction magnets is shown in Fig. 1, where the first extraction quadrupole QDEX1A is placed 6 m after the IP and 0.29 m behind the QD0. In this solution, the QD0 and the extraction pipe are placed in the same cryostat as shown in Fig. 2.

One disadvantage of this solution is that the extraction focusing starts later after IP which tends to increase the beam size in the extraction quadrupoles. However, in this design it was possible to increase the gradient of the QDEX1A quadrupole [7] and reduce the effect of missing focusing.

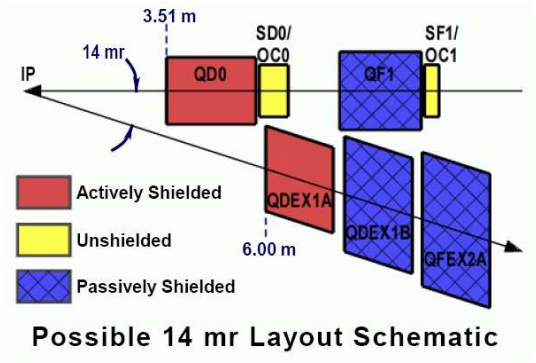

Figure 1: Schematic of the 14 mrad crossing with the incoming and extraction magnets on one side of IP.

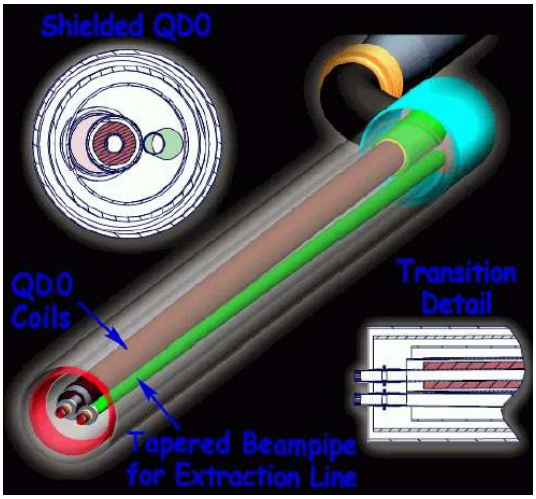

Figure 2: Design drawing of the nearest to IP incoming quadrupole QD0 and the extraction beam pipe in a cryostat.

The optics and lattice functions in the 14 mrad extraction line are shown in Fig.3, where the IP is at $s=0$ and the dump is at ≈ 400 m. As in the 20 mrad design, the optics consists of the initial DFDF focusing system, followed by two vertical chicanes for energy and polarization diagnostics, and a long drift to the dump with three collimators.

The first three extraction quadrupoles will be superconducting and are placed between s = 6 m and 11.5 m from IP. They are followed by the 4 m dedicated drift to provide transverse space for the incoming crab cavity, and the warm extraction magnets starting at s = 15.5 m. The diagnostic energy and polarization chicanes create the maximum vertical offset and dispersion of 1.7 and 2 cm, respectively. The optics provides the 2nd focal point at the center of the polarimeter chicane at s$\approx$ 148 m to attain the required

* Work supported by the Department of Energy Contract DE-AC02-76SF00515.

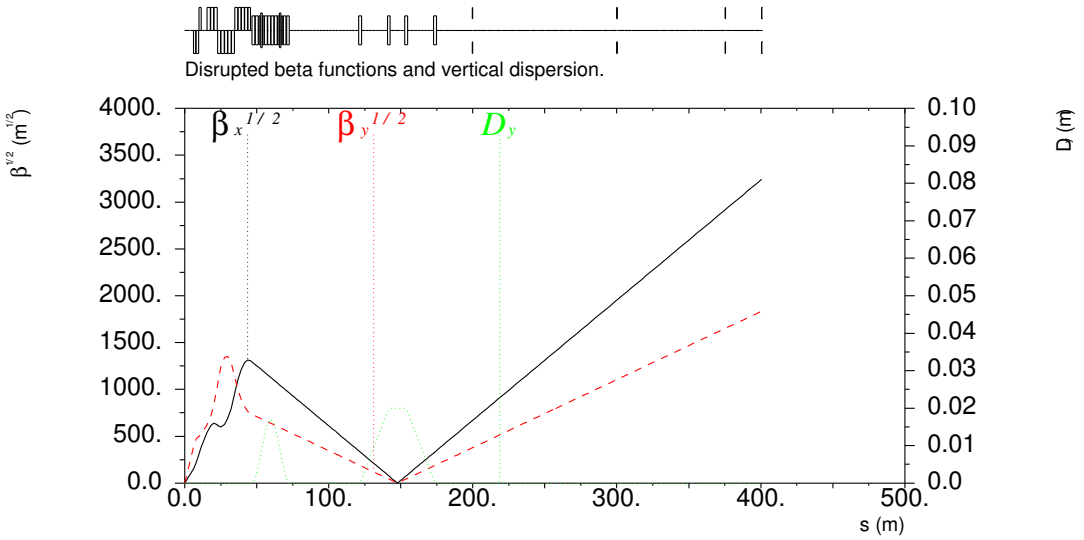

Figure 3: Disrupted beta functions and vertical dispersion in the 14 mrad extraction line. IP is at s = 0.

$< 100\mu$m beam size. The horizontal angular transformation term $R_{22} = -0.503$ from IP to the 2nd focus is made close to one of the optimum values (± 0.5) for polarization measurement. The diagnostic scheme for the 14 mrad extraction is the same as for the 20 mrad design which can be found in [9] and [3].

In addition to the disrupted electron and BS photon beams, the extraction dump must also accept the full undisrupted beam if there is no collision at IP. However, without the disruption, the beam size at the end of last extraction magnet is still too small for the dump window. The final 226 m drift is included to naturally increase the undisrupted beam size in order to avoid damage to the dump window. However, the long drift also increases the larger sizes of the disrupted electron and photon beams. In order to fit the disrupted beam sizes to the specified 15×15 cm size of the dump window [8], the three collimators are placed at s$\approx$200 m, 300 m and 375 m.

The extraction apertures are made sufficiently large to avoid large losses on the extraction magnets. Because of the large energy spread in the disrupted beam, most of the losses occur in the very low energy tail due to overfocusing in quadrupoles. For the ILC beam parameter options [12, 13], the size of the quadrupole aperture is dominated by the electron beam size. But in the chicane bends which are farther from the IP the photon aperture becomes larger. Because the photons follow the straight lines, the photon aperture linearly increases with distance and can be rather large. In the 14 mrad design, we studied two options for the photon aperture in magnets. In the first option, the magnet apertures were set to accept the photons with the maximum angle of ± 1.25 mrad at IP. This angle corresponds to the maximum photon angle at IP for the ILC nominal and high luminosity options as descussed below. Therefore, no photon loss on magnets is expected in this case. Note that there will be losses on final collimators which are set to limit the beam size at the dump window. In the second option, the magnet apertures were set to accept the photons with the maximum angle of ± 0.75 mrad at IP. In this option, the magnets at a large distance have smaller and more practical apertures. In addition, this aperture size is favoured for the diagnostics [9]. Fig. 4 shows the schematic of the these two aperture models.

The parameters of the 14 mrad extraction quadrupoles are shown in Table 1 for the 1 TeV center of mass (CM) energy. At 0.5 TeV CM, the magnet field will be lower a factor of 2. All the bends in the diagnostic chicanes are 2 m long with 0.8339 T field at 1 TeV CM.

Table 1: Quadrupole parameters at 1 TeV CM.

Name	L [m]	B′ [T/m]	R [mm]
QDEX1A	1.6407	-83.333	18
QDEX1B	1.6407	-50.000	24
QFEX2A	1.6187	+40.000	30
QFEX2B,2C,2D	2.1431	+23.809	42
QDEX3A,3B	2.1058	-23.809	42
QDEX3C	2.1058	-21.739	46
QDEX3D	2.1058	-19.231	52
QDEX3E	2.1058	-16.129	62
QFEX4A	1.9448	+14.084	71
QFEX4B,4C,4D,4E	1.9448	+11.765	85

PARTICLE TRACKING

Simulation of beam transport from IP to dump was performed using the DIMAD code[10]. Beam distributions of up to $3.5 \cdot 10^7$ disrupted e^+ and e^- at IP were generated using the GUINEA–PIG code[11] for the ILC "nominal" and "high luminosity" options of beam parameters [12] and for the two alternative 1 TeV CM high luminosity options [13]. Distributions of the BS photons were also generated for each option. In addition, two cases were con-

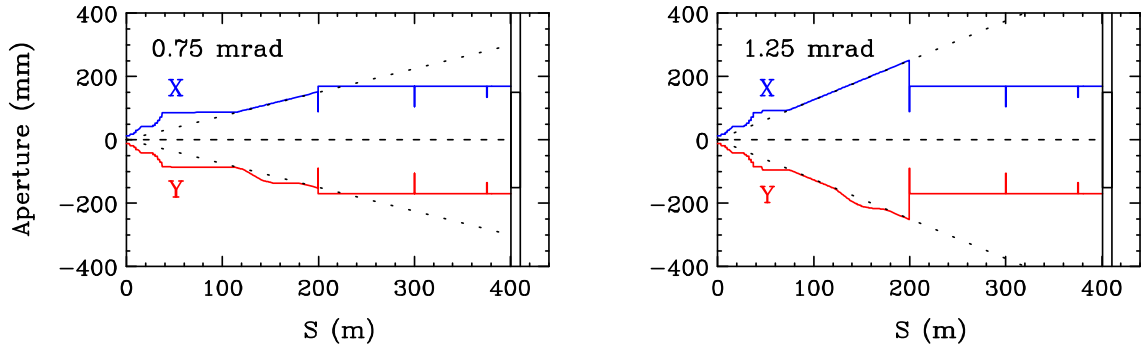

Figure 4: Two models of extraction aperture providing acceptance for the BS photons with the maximum IP angle of ± 0.75 mrad and ± 1.25 mrad. Three collimators at s $>$ 200 m limit the beam size to ± 15 cm at dump window.

sidered: 1) ideal beam collisions, and 2) collisions with a large vertical beam-to-beam offset Δy which increases the vertical divergence in both the primary and BS photon beams. The value of Δy was selected to maximize the divergence. Summary of the disrupted beam parameters in these options is presented in Table 2. The shown maximum IP angles and energy spread are the important parameters affecting the beam loss. Note that the beam divergence and energy spread in the high luminosity cases "c15" and "c25" are large compared to the nominal options. The two alternative high luminosity cases "c26" and "c27" are designed to reduce the energy spread, but at the cost of somewhat lower luminosity. One can see that at ideal collisions the disrupted beam size is larger in the horizontal plane, but the vertical size can dominate at a large Δy. The low energy tail increases with the beam energy and luminosity. The disrupted energy distributions for the 0.5 TeV CM and 1 TeV CM options are shown in Fig. 5.

As mentioned earlier, the dump must accept the full undisrupted beam. The Table 3 shows the x and y rms sizes of the undisrupted primary beam at the dump at s$\approx$400 m. The beam spot of $\sigma_x\sigma_y > 1.7$ mm^2 appears acceptable for survival of the dump window [8]. However, a significantly larger size ($\sim$70 mm^2) is required to satisfy the specifications for water boiling in the dump vessel [8]. We consider that the larger beam size can be achieved by using a rastering system before the dump for sweeping the bunches over a wider area on the dump.

Table 3: Undisrupted beam size at dump for various ILC beam options.

CM energy	σ_x [mm]	σ_y [mm]	$\sigma_x\sigma_y$ [mm^2]
0.5 TeV nominal (c11)	3.97	0.43	1.71
0.5 TeV high-L (c15)	5.75	0.52	2.97
1.0 TeV nominal (c21)	2.35	0.78	1.84
1.0 TeV high-L (c25)	4.06	0.79	3.21
1.0 TeV high-L (c26)	2.35	0.75	1.77
1.0 TeV high-L (c27)	2.77	0.75	2.06

Summary of the beam loss in extraction magnets and collimators is presented in Tables 4 and 5 for the 1.25 mrad and 0.75 mrad photon apertures. The detailed distribution of primary beam losses within the range of extraction magnets (prior to collimators) is shown in Fig. 6–16. The detector solenoid is not included in the calculation, but the earlier studies [3] showed that it has a small effect on beam loss if the orbit created in the solenoid is corrected.

To be continued ...

CONCLUSION

To be included ...

REFERENCES

[1] Y. Nosochkov, *et al.*, SLAC–PUB–11363 (2005), presented at the LCWS 2005, Stanford, CA, USA (2005).

[2] R. Appleby, *et al.*, SLAC–PUB–11372 (2005), presented at the LCWS 2005, Stanford, CA, USA (2005).

[3] Y. Nosochkov, *et al.*, SLAC–PUB–11205 (2005), presented at the PAC 2005, Knoxville, TN, USA (2005).

[4] Y. Nosochkov, *et al.*, presented at the Snowmass ILC Workshop 2005, Snowmass, CO, USA (2005), http://alcpg2005.colorado.edu:8080/alcpg2005/program/accelerator/WG4/aug17_nosochkov_extraction20mrad.pdf .

[5] Y. Nosochkov for the SLAC-BNL-UK-France Task Force, presented at the Snowmass ILC Workshop 2005, Snowmass, CO, USA (2005), http://alcpg2005.colorado.edu:8080/alcpg2005/program/accelerator/WG4/aug17_nosochkov_extraction2mrad.pdf .

[6] B. Parker, *et al.*, "Compact Superconducting Final Focus Magnet Options for the ILC," presented at the PAC 2005, Knoxville, TN, USA (2005).

[7] B. Parker, "Recent Progress Designing Compact Superconducting Final Focus Magnets for the ILC," these proceedings.

[8] D. Walz, presented at the Snowmass ILC Workshop 2005, Snowmass, CO, USA (2005), http://alcpg2005.colorado.edu:8080/alcpg2005/program/accelerator/WG4/aug17_beam_dump_d_walz.pdf .

[9] K.C. Moffeit, *et al.*, SLAC–PUB–11322 (2005), presented at the LCWS 2005, Stanford, CA, USA (2005).

[10] http://www.slac.stanford.edu/accel/ilc/codes/dimad/ .

[11] D. Schulte, "Beam-Beam Simulations with GUINEA–PIG," ICAP98, Monterey, CA, USA (1998).

[12] T. Raubenheimer, http://www-project.slac.stanford.edu/ilc/acceldev/beamparameters.html (February 28, 2005).

Table 2: Parameters of disrupted beam at IP for various ILC beam options.

CM energy	Luminosity $[10^{38}]$ $[\mathrm{m}^{-2}\mathrm{s}^{-1}]$	Beam power [MW]	Δy offset [nm]	Primary electrons			BS photons	
				E_{min}/E_0 [%]	X'_{max} [μrad]	Y'_{max} [μrad]	X'_{max} [μrad]	Y'_{max} [μrad]
0.5 TeV nominal (c11)	2.03	11.3	0	36	529	253	369	212
			200	36	474	674	366	537
0.5 TeV high-L (c15)	4.92	11.3	0	17	1271	431	723	320
			120	17	1280	1415	782	1232
1.0 TeV nominal (c21)	2.81	18.1	0	20	496	159	271	148
			100	19	423	566	279	408
1.0 TeV high-L (c25)	7.81	18.1	0	6.3	2014	489	937	296
			80	6.2	1731	1592	974	1200
1.0 TeV high-L (c26)	5.72	21.7	0	15	661	249	338	170
			100	14	598	696	376	585
1.0 TeV high-L (c27)	4.64	18.1	0	15	597	236	546	159
			100	14	537	691	342	532

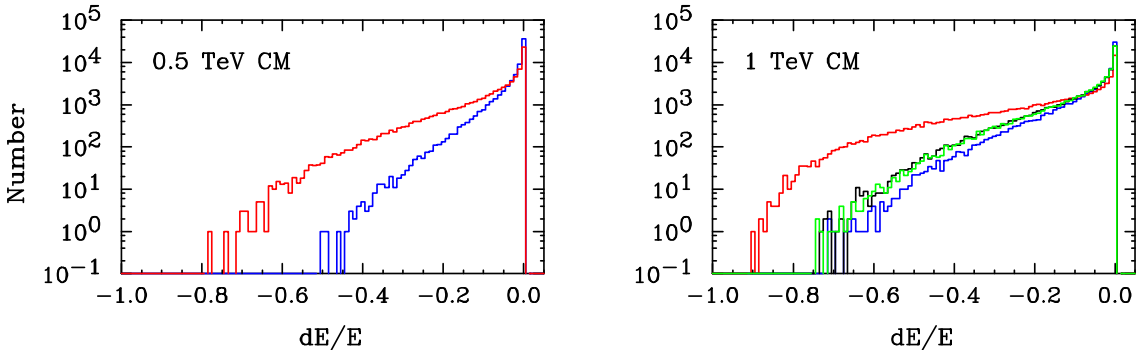

Figure 5: Energy distribution of disrupted beam at IP for various ILC beam options.

[13] A. Seryi, presented at the Snowmass ILC Workshop 2005, Snowmass, CO, USA (2005), http://alcpg2005.colorado.edu:8080/alcpg2005/program/accelerator/GG1/aug17_seryi_high_lumi_pars.ppt .

Table 4: Power loss of disrupted beam in the extraction line for 1.25 mrad photon aperture.

CM energy	Δy offset [nm]	Total electron loss (kW)				Total BS photon loss (kW)				Electron loss on SC quads [kW]
		Prior to collim.	Collimators			Prior to collim.	Collimators			
			1	2	3		1	2	3	
0.5 TeV nominal (c11)	0	0	0	1.3	0.88	0	0	0.002	0	0
	200	0.0004	3.0	17	0.45	0	0.09	13	0	0
0.5 TeV high-L (c15)	0	1.3	39	228	45	0	1.8	28	0	0.002
	120	5.2	372	475	32	0	137	195	0	0
1.0 TeV nominal (c21)	0	0.11	0.55	0.47	0	0	0	0	0	0
	100	1.4	1.4	5.9	0.43	0	0	0.17	0	0
1.0 TeV high-L (c25)	0	80	54	372	60	0	1.2	7.2	0	0.55
	80	213	395	1077	40	0	48	276	0	0.58
1.0 TeV high-L (c26)	0	0.93	3.1	1.3	1.6	0	0	0	0	0
	100	6.4	6.5	95	2.1	0	0.07	2.1	0	0
1.0 TeV high-L (c27)	0	0.66	1.3	1.0	0.15	0	0	0.003	0	0
	100	4.1	6.1	59	2.0	0	0.04	0.90	0	0

Table 5: Power loss of disrupted beam in the extraction line for 0.75 mrad photon aperture.

CM energy	Δy offset [nm]	Total electron loss (kW)				Total BS photon loss (kW)				Electron loss on SC quads [kW]
		Prior to collim.	Collimators			Prior to collim.	Collimators			
			1	2	3		1	2	3	
0.5 TeV nominal (c11)	0	0	0	1.3	0.88	0	0	0.002	0	0
	200	0.0009	3.0	17	0.45	0	0.09	13	0	0
0.5 TeV high-L (c15)	0	2.0	38	228	45	0	1.8	28	0	0.002
	120	15.5	361	475	32	0.48	136	195	0	0
1.0 TeV nominal (c21)	0	0.25	0.38	0.47	0	0	0	0	0	0
	100	2.3	0.80	6.0	0.42	0	0	0.17	0	0
1.0 TeV high-L (c25)	0	105	31	372	60	0.013	1.2	7.2	0	0.55
	80	256	348	1076	39	0.99	47	276	0	0.58
1.0 TeV high-L (c26)	0	1.8	1.6	1.3	1.6	0	0	0	0	0
	100	10.2	3.3	94	3.7	0	0.07	2.1	0	0
1.0 TeV high-L (c27)	0	1.3	0.74	1.0	0.15	0	0	0.003	0	0
	100	6.7	3.8	59	1.8	0	0.04	0.90	0	0

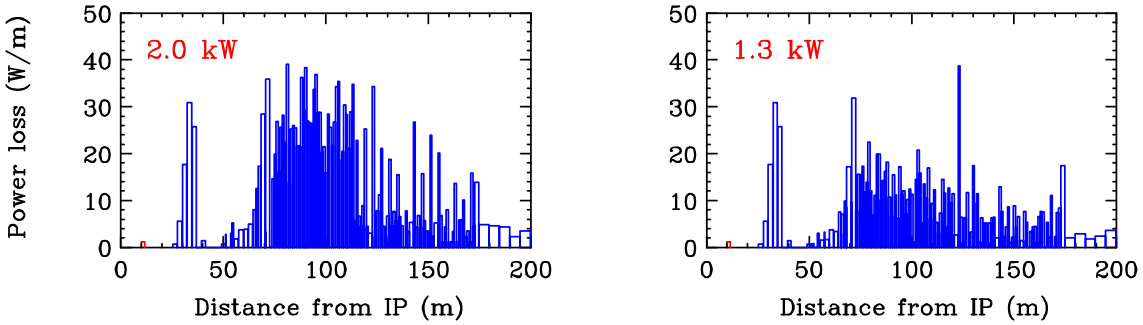

Figure 6: Primary beam loss for 0.5 TeV CM high luminosity (c15), $\Delta y = 0$, and 0.75 mrad (left) and 1.25 mrad (right) photon aperture.

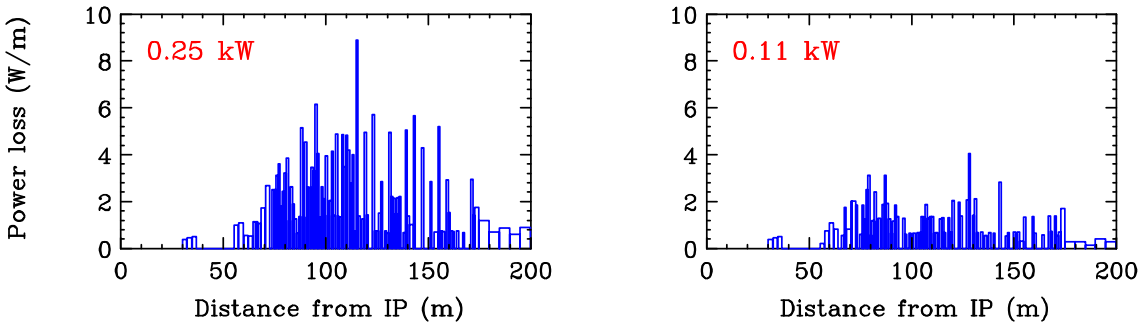

Figure 7: Primary beam loss for 1.0 TeV CM nominal luminosity (c21), $\Delta y = 0$, and 0.75 mrad (left) and 1.25 mrad (right) photon aperture.

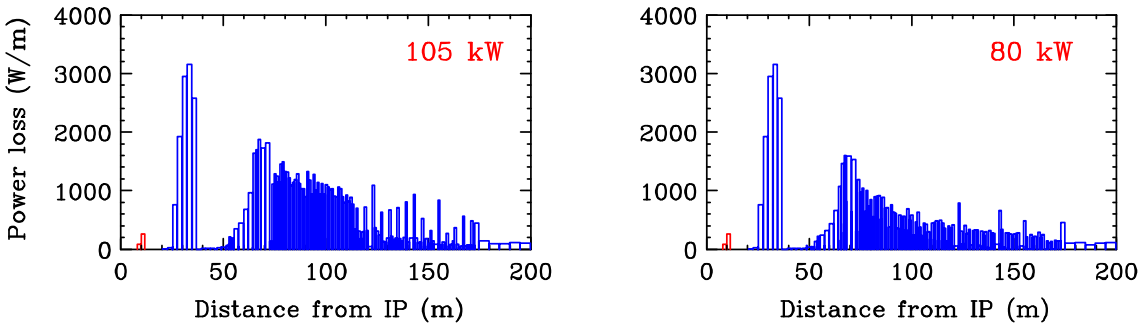

Figure 8: Primary beam loss for 1.0 TeV CM high luminosity (c25), $\Delta y = 0$, and 0.75 mrad (left) and 1.25 mrad (right) photon aperture.

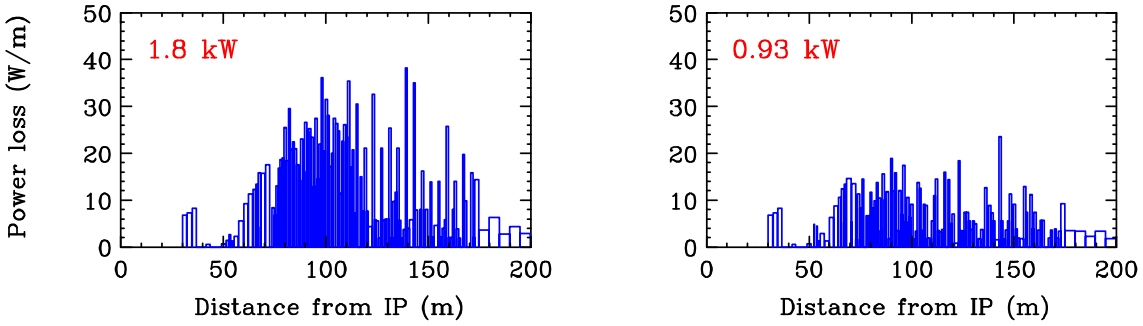

Figure 9: Primary beam loss for 1.0 TeV CM high luminosity (c26), $\Delta y = 0$, and 0.75 mrad (left) and 1.25 mrad (right) photon aperture.

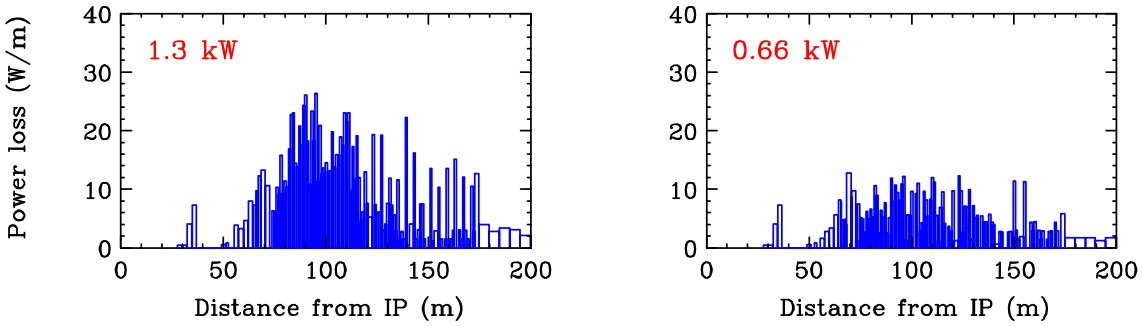

Figure 10: Primary beam loss for 1.0 TeV CM high luminosity (c27), $\Delta y = 0$, and 0.75 mrad (left) and 1.25 mrad (right) photon aperture.

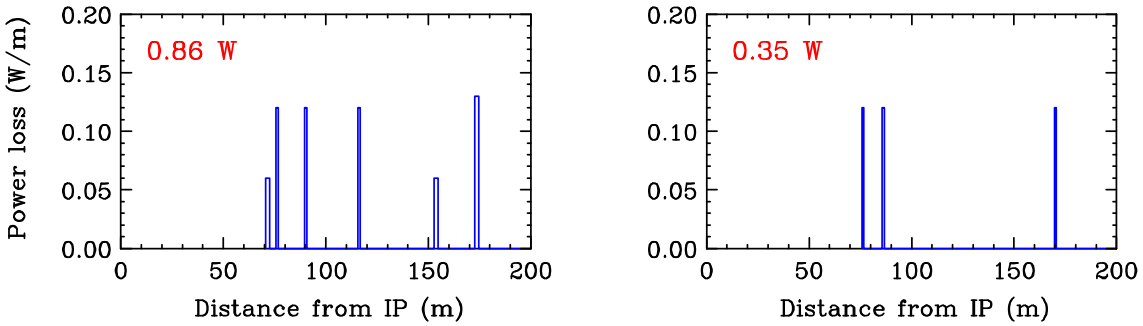

Figure 11: Primary beam loss for 0.5 TeV CM nominal luminosity (c11), $\Delta y = 200$ nm, and 0.75 mrad (left) and 1.25 mrad (right) photon aperture.

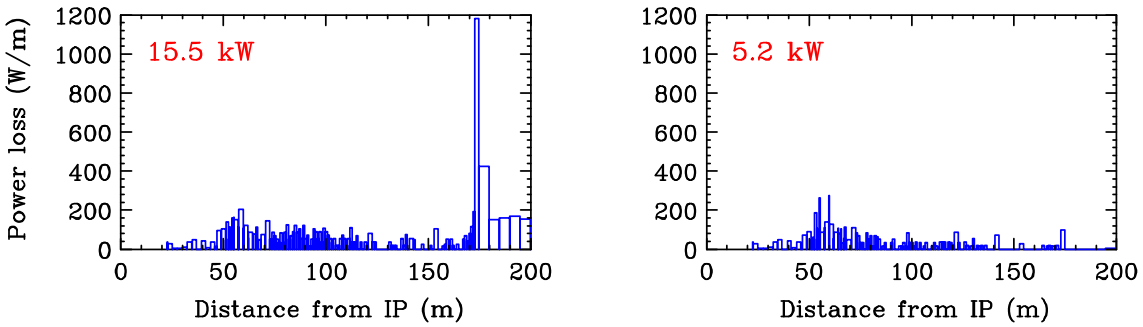

Figure 12: Primary beam loss for 0.5 TeV CM high luminosity (c15), $\Delta y = 120$ nm, and 0.75 mrad (left) and 1.25 mrad (right) photon aperture.

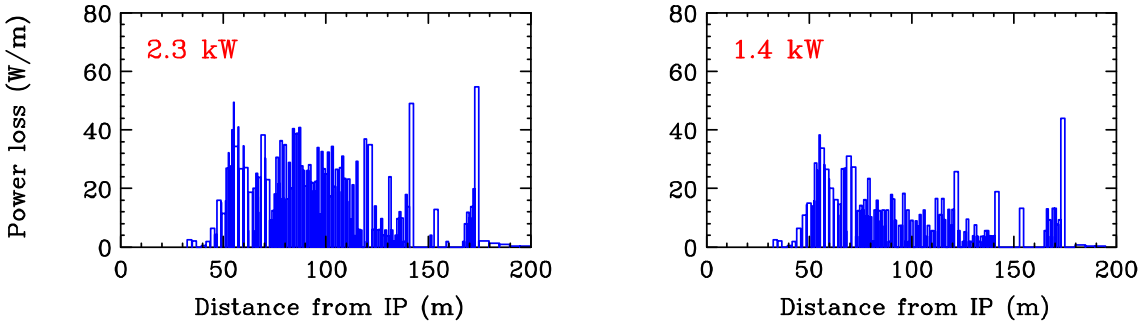

Figure 13: Primary beam loss for 1.0 TeV CM nominal luminosity (c21), $\Delta y = 100$ nm, and 0.75 mrad (left) and 1.25 mrad (right) photon aperture.

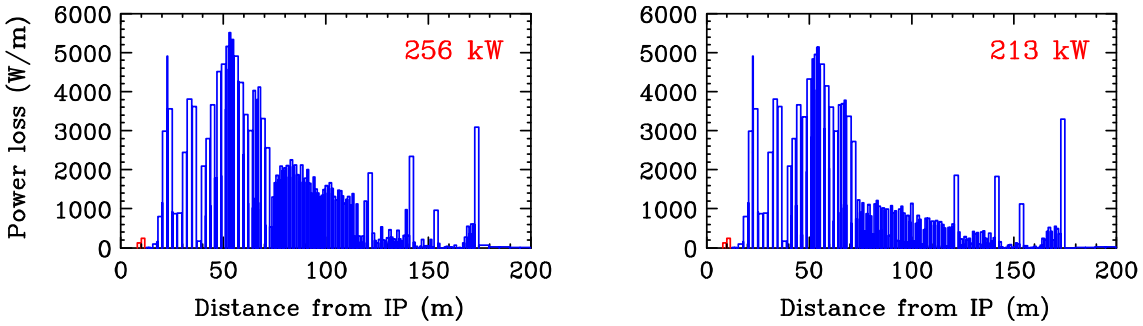

Figure 14: Primary beam loss for 1.0 TeV CM high luminosity (c25), $\Delta y = 80$ nm, and 0.75 mrad (left) and 1.25 mrad (right) photon aperture.

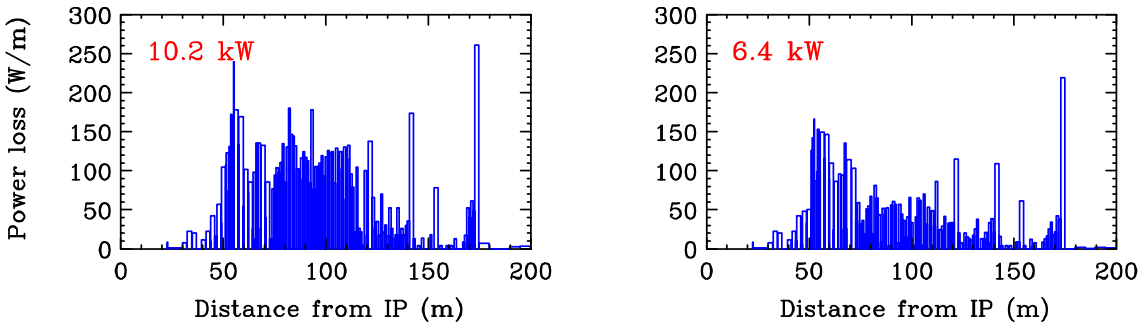

Figure 15: Primary beam loss for 1.0 TeV CM high luminosity (c26), $\Delta y = 100$ nm, and 0.75 mrad (left) and 1.25 mrad (right) photon aperture.

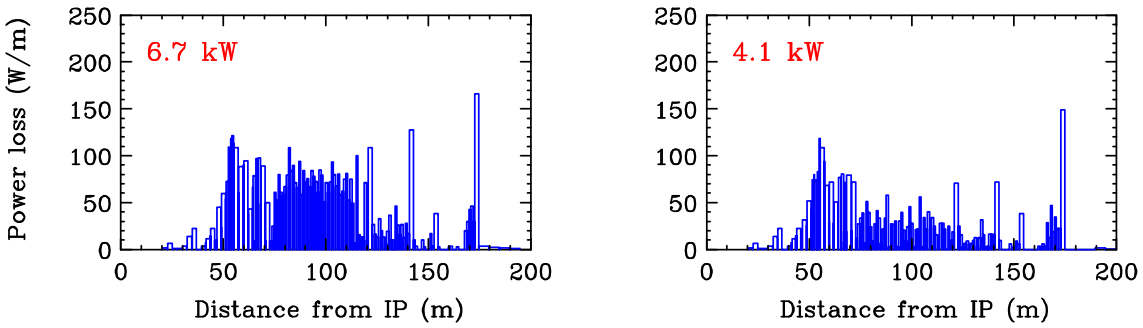

Figure 16: Primary beam loss for 1.0 TeV CM high luminosity (c27), $\Delta y = 100$ nm, and 0.75 mrad (left) and 1.25 mrad (right) photon aperture.